Electronic properties of Fe impurities in SnS van der Waals crystals – revealing high-mobility holes

J. Navrátil[1], O. Caha[2], J. Kopeček[3], P. Čermák[1], J. Prokleška[4], V. Holý[2,4], V. Sechovský[4], L. Beneš[1], K. Carva[4], J. Honolka[3], Č. Drašar[1]

[1] *University Pardubice,Faculty of Chemical Technology, Studentská 573, 532 10 Pardubice, Czech Republic*

[2]*Department of Condensed Matter Physics, Masaryk University, Kotlarska 2, 61137 Brno, Czech Republic*

[3] *Institute of Physics of the Czech Academy of Sciences, Na Slovance 2, 182 21 Prague, Czech Republic*

[4] *Department of Condensed Matter Physics, Faculty of Mathematics and Physics Charles University, Ke Karlovu 5, 121 16 Prague, Czech Republic.*

Keywords: p-type SnS, single crystal, semiconductor, doping, electrical properties.

Abstract

Defect control is critical to achieve long carrier lifetimes in semiconductors. SnS is a promising thermoelectric and photovoltaic material. In this study, we investigated Fe doping in a series of single crystals of $Sn_{1-x}Fe_xS$ up to concentrations of x = 0.05. The integration of Fe atoms into the host matrix has been investigated using several methods. Although the doped single crystals appear rather disordered, the hole mobility is very high (~8500 $cm^2V^{-1}s^{-1}$ for $Sn_{0.99}Fe_{0.01}S$), suggesting that the hole-mediated charge transport in this material is largely insensitive to impurities. Charge transport analysis suggests that the incorporation of Fe atoms leads to the healing of the intrinsic defect structure and the exclusion of minority electrons from charge transport, allowing the observation of high hole mobility.

Introduction

Tin (II) chalcogenides (SnSe and SnS) have attracted considerable attention in recent decades because of their great potential in many areas of materials science, such as photovoltaics[1,2], optoelectronics[3,4], batteries, supercapacitors[5,6], and especially thermoelectrics[7,8]. While

the compound SnSe has been subject of extensive literature since its discovery as a cutting-edge thermoelectric material[9],[10], other isostructural member of the family (SnS) is only beginning to be explored. Recent interest is especially due to economic considerations, for its potential use as an earth-abundant semiconductor.

Tin monosulfide (SnS) is a natural p-type semiconductor (with an indirect band gap of 1.08 eV[11]) with hole densities between 10^{15} and 10^{18} cm^{-3} and quite high hole mobilities (up to 100 $cm^2/(V.s)$ at 300 K)[12]. The high optical absorption coefficients at photon energy above 1.3 eV, low production costs, long-term stability make SnS a potentially suitable material for photovoltaic and sensor applications[13]. Unique properties can be achieved by the formation of van der Waals (vdW) heterojunctions/heterostructures of SnS with other 2D semiconductors, e.g. MoS_2 [14], SnS_2[15] or GeS[5], potentially useful for the realization of novel electronic, optoelectronic, and valleytronic devices. Recently, significant efforts have been made in the research of p-n SnS homojunction devices and high-efficiency multi-junction SnS solar cells[16].

Achieving control over the transport properties and conductivity type of SnS is essential for advancing the above concepts. Therefore, it is important to understand the role of individual dopants and their interactions with the intrinsic point defects of the host compound. Both tin vacancies (V_{Sn}) and sulphur vacancies (V_S) are present in pristine SnS[17]. Its overall p-type behavior is based on the fact that doubly ionized V_S, recognized as a deep-level donor cannot compensate for the acceptor contribution of shallow V_{Sn} levels [16].

In this work, we present a study on the structural and electronic properties of Fe-doped SnS single crystals (concentration of diluted Fe up to 0.6 at %.) grown by free-melt cooling (FMC) Fe alters the defect structure of SnS in a way that virtually eliminates minority electron carriers from transport. This allows predominant hole transport to be observed. Interestingly, the holes show high mobility in the doped sample, suggesting that the hole charge transport in this material is largely insensitive to impurities. High mobility was maintained despite the increased mosaicity of the doped samples. Thus far, magnetically doped Sn chalcogenides have only been addressed theoretically. Theoretical works[18,19] have concluded that the implementation of magnetic degrees of freedom of (Mn, Fe, or Co) atoms may be promising for spintronic and magneto-optic applications. However, the diversity of Fe-incorporation in SnS makes magnetism analysis quite difficult and requires the investigation of large sample sets.

Results and discussion

HRXRD analysis

It is known that the properties of vdW materials doped with 3d transition metals are very sensitive to changes in growth parameters and stoichiometry[20]. In particular, at high concentrations of 3d transition metals, inhomogeneous phases may appear owing to the solubility limitation of 3d metal[21–24]. In this paper, we present a study on Fe-doped SnS single crystals.

The structural and stoichiometric properties of the samples were characterized using powder and high-resolution X-ray diffraction and energy-dispersive x-ray analysis (PXRD, HRXRD, and EDX). From the PXRD patterns obtained for the $Sn_{1-x}Fe_xS$ powder prepared from single crystals (SCs) (x=0-0.1), we found that for $x \geq 0.05$, a secondary FeS phase started to appear (see Fig. S1 in SI). The presence of the hexagonal troilite phase in SnS single crystals was also confirmed by the EDX/EBDS technique for $Sn_{0.95}Fe_{0.05}S$ (see Fig. 4), but an FeS-like phase is likely to be present within the SnS matrix already at the lowest Fe doping concentration (see Fig. 3). However, both STM[25] and EDX experiments (below) suggest that part of the Fe was diluted in the SnS structure. Accordingly, the results presented below for the transport properties of Fe-doped SnS crystals suggest that Fe-related point defects interact with internal defects and strongly alter their transport properties (see the discussion below). An additional foreign SnS_2 phase was detected by HRXRD (inset in Fig. 1) in FMC $Sn_{0.99}Fe_{0.01}S$. In contrast, the undoped FMC SnS has a perfect structure with no detected foreign phases. Note that we however have observed SnS_2 in the undoped SnS reference samples (Fig. 1) prepared by the Bridgman method (BM). This suggests that the formation of SnS_2 (001) is an intrinsic material property of the SnS host structure, which critically depends on the growth conditions[11,26,27]. Specifically, the BM method, unlike the FMC method, essentially involves directional solidification with large temperature gradients. Therefore, we chose the FMC method for further study. From the broad weak peak of SnS_2(001) in the reciprocal space maps around the SnS(020) diffraction peaks (Fig. S2), the thickness of such an inclusion was estimated to be 20 - 40 nm. We also observed the formation of the SnS_2 impurity phase in the Fe-doped SnS FMC sample $Sn_{0.99}Fe_{0.01}S$ (Fig. 1), suggesting that Fe impurities may promote SnS_2 formation.

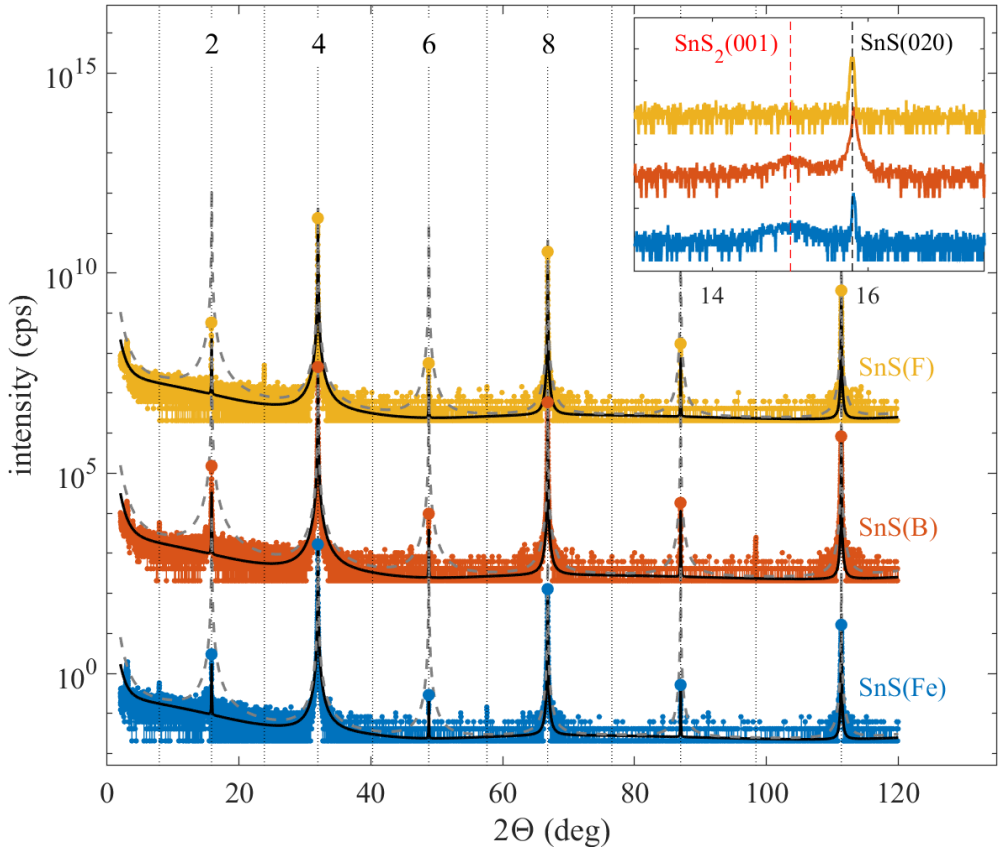

Figure 1: Results of x-ray diffraction measurements – experimental symmetric 2θ/ω scans of pure SnS samples denoted SnS(F) and SnS(B) as well as the Fe-doped sample (points). The scans were measured along the 0*K*0 line in reciprocal space, the vertical dotted lines denote the positions of the maxima, the parameter of the lines is the 2nd diffraction index K. The full and dashed black lines display the results of simulations for two various SnS orthorhombic structures denoted I (PDF-04-004-3838 – full lines) and II (PDF-00-039-0354 – dashed lines). From the comparison it is obvious that the structure of the samples well corresponds to the published structure I. The inset displays the region around the SnS(020) maximum; the broad maximum at approx. 15.5 deg corresponds to a SnS_2(001) diffraction peak. SnS(F) and SnS(Fe) denote SCs prepared by FMC method, SnS(B) denotes undoped SnS SC prepared by the Bridgman method.

From the Cohen-Wagner plots of the SnS (0*K*0) diffraction maxima for K = 4,8,12 (see SI Fig. S3), we derived a lattice constant b = (11.192 ± 0.002) Å for all the samples examined, which is larger than the published value of 11.143 Å. We did not observe any significant changes in b due to Fe doping, consistent with the low impurity concentration and similar ionic radii of Fe^{2+}(0.76 Å) and Sn^{2+}(0.93 Å)[28]. However, this may not be entirely consistent with the interstitial position in the center of the vdW gap. Indeed, our recent work suggests that Fe impurities predominantly enter structurally relaxed interstitial positions[25].

The quality of a single crystal can be assessed using reciprocal space maps (Fig. 2). From the broadening of the diffraction maxima along the horizontal Q_x axis, we determined the angular mosaic spread in all samples to be approximately 1° or more for FMC SnS(Fe), 0.13° for BM -SnS(B), and 0.03° for FMC - SnS(F). The maximum width along the vertical Q_z axis is influenced by the size of the mosaic blocks and by a possible strain gradient in the blocks; if we neglect the latter effect, the mosaic-block size can be estimated to be 200-300 nm. The upper figure of Fig. 2 shows that in the case of the Fe-doped SC ($Sn_{0.99}Fe_{0.01}S$), this method revealed a substantial increase in mosaicity, that is, the formation of a nanostructure due to small variations in the tilt of the trigonal axis c along the ab planes.

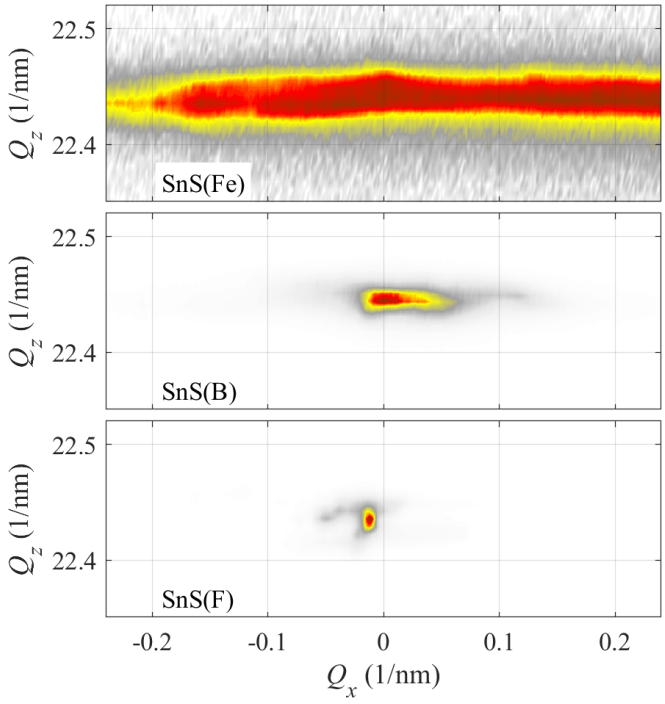

Figure 2: Reciprocal-space maps around the diffraction peaks SnS(040) of samples iron doped SnS (Fe), SnS - Bridgman method (B), and SnS – free-melt cooling (F), top to bottom. The color coding is logarithmic and the colors from white to dark red span over four decades.

SEM -EDX analysis and magnetic properties

Electron backscatter diffraction (EBSD), spatially resolved energy-dispersive X-ray analysis (EDX), and magnetic properties were used to investigate the influence of Fe integration on the bulk sample properties.

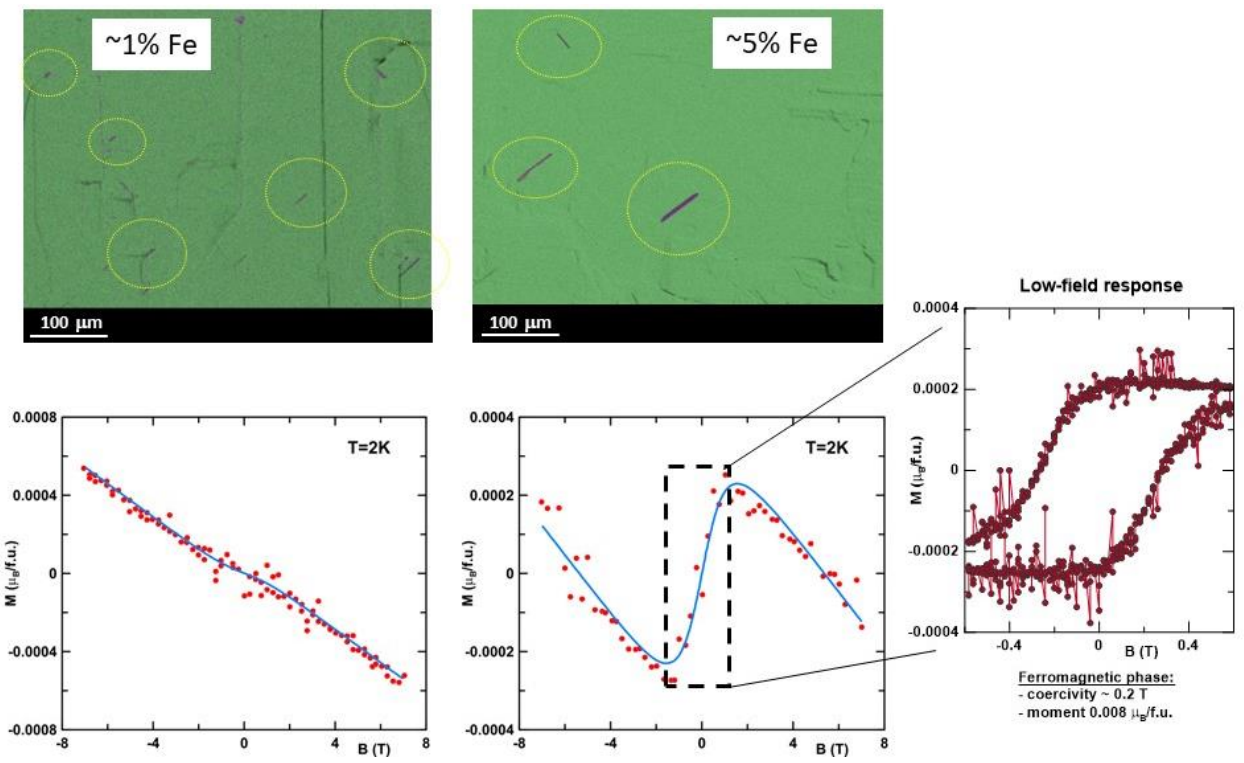

Figure 3: EDX-SQUID: EDX and SQUID results for Fe:SnS with Fe concentrations x = 0.01 and x = 0.05. (a) and (b) EDX contrast of cleaved surfaces revealing elongated Fe-rich areas (violet color, marked by yellow circles) with 90 deg mutual orientation, which are embedded in green areas of low Fe content. (c) and (d) show respective magnetization data taken at T = 2K. The inset at the right shows the magnetic coercivity for x = 0.05 in detail.

To study the enhanced mosaic-block formation and possible phase separations in the presence of x = 0.01 Fe, we utilized spatially resolved EBSD and EDS to study samples with considerably higher and lower Fe concentrations than x = 0.01. Fig. 3 summarizes spatially resolved 500µm x 500µm element maps from cleaved SnS(Fe) surfaces for x = 0.001 and x = 0.05, where the color coding represents the local Sn, S, and Fe atomic concentrations. Homogeneous green areas correspond to the expected Sn:S ratios of approximately 1:1 and a low Fe concentration. However, in addition, a few Fe-rich platelets of elongated shape are visible in violet color, typically 20 - 50 µm long. A comparison of the platelets for the x = 0.001 and x = 0.05 samples in Fig. 3 (a) and (b) suggests that higher nominal Fe concentrations lead to fewer but longer and wider Fe-rich platelets during FMC growth. We note that these platelets are strictly locked to the crystal axes of the SnS host structure and, therefore, do not represent a random inclusion of foreign phase clusters. The platelets were mostly aligned in the SnS[010] direction, but 90 deg rotated alignments were also visible. This finding suggests the epitaxial growth of the foreign phase. Fig. 3 (c) and (d) show the magnetization measurements for x = 0.01 and x = 0.05. The magnetization curve in Fig. 3 (d) shows an apparent coercive field attributable to troilite inclusions[29,30] as evidenced by the EDX - EBDS

experiment. Fig. 4 summarizes the results of the analysis performed on the sample with x = 0.05. The foreign phase forms thin platelets with a thickness of several hundreds of nanometers (density of 5 - 10 cluster/mm^2) with an areal coverage of < 0.5%. Both the EDX and EBDS (local Kikutchi patterns) analysis indicate FeS troilite phase for foreign phase inclusions and SnS orthorhombic structure for matrix. Importantly, the SnS matrix contained 0.6 ± 0.1 at. % of Fe.

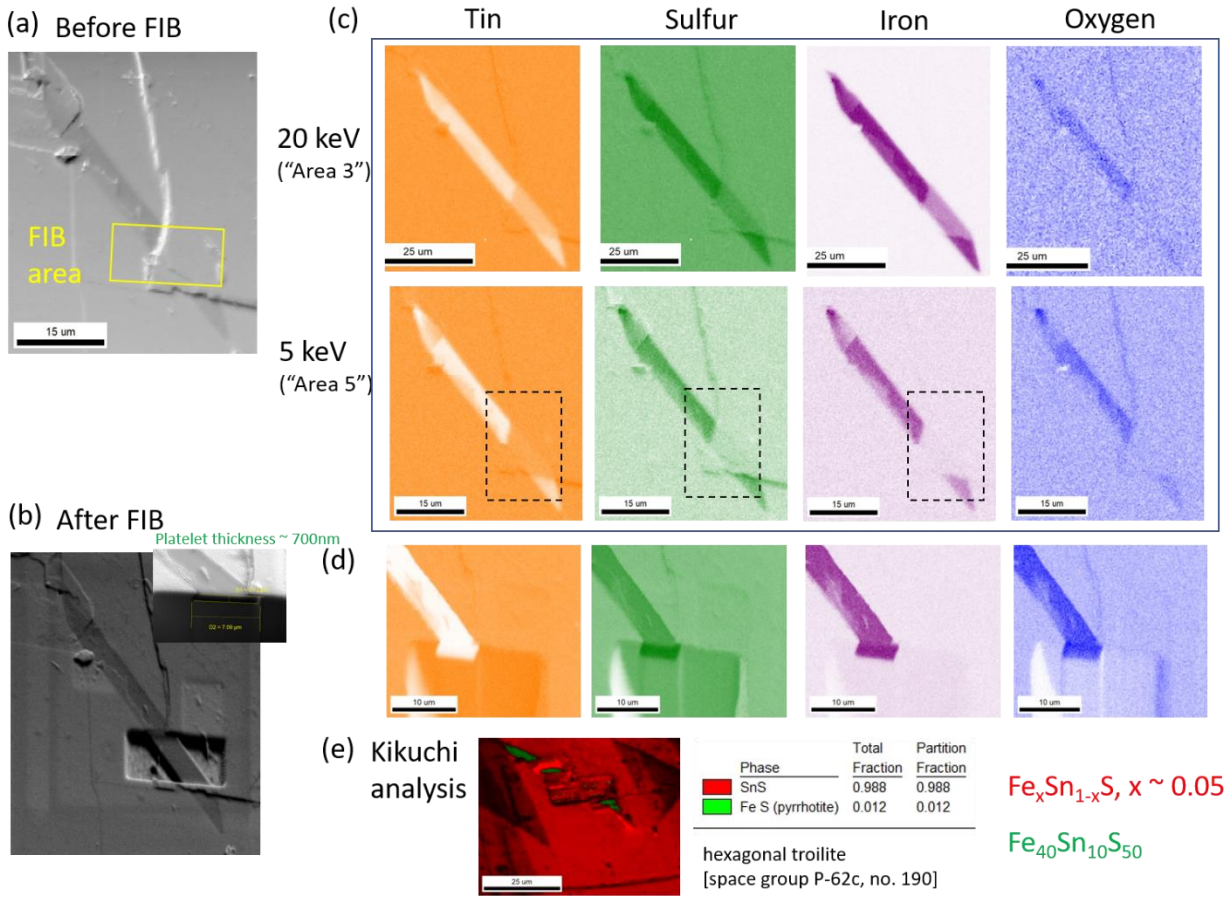

Figure 4: EDX and EBSD analysis of Fe-rich platelets on Fe:SnS with x=0.05. (a) and (b) show the sample surface before and after FIB through an Fe-rich platelet. The FIB area is marked by a yellow square in (a). (c) and (d) show EDX maps at different electron energies before and after FIB treatment. (e) Analysis of the local Kikuchi patterns derived from EBSD, revealing a FeS hexagonal troilite structure [space group P-62c, no. 190] on the platelet, and SnS(001) in the surrounding matrix.

XAFS experiments

In Fig. 5 the EXAFS data of Fe:SnS with x = 0.01 are presented together with simulations (codes FDMNES and FEFF) for Fe in several crystal forms - bulk phases FeS_2 and FeS (hexagonal and tetragonal), or as diluted atoms in SnS, assuming Fe_i in vdW (relaxed and unrelaxed) and Fe_{Sn} substitutional position – see Fig.5 (e) –(g). The comparison shows that the interstitial Fe in SnS in

the relaxed vdW positions (Fe_i) and bulk hexagonal FeS (troilite structure) match the experiment reasonably well, both corresponding to nearest neighbor (NN) Fe-S distances of approximately 2.45 Å. In contrast, bulk FeS_2 or tetragonal FeS phases, as well as substitutional Fe_{Sn} or Fe_i impurities in the central vdW positions (unrelaxed vdW position) are not observed in significant amounts.

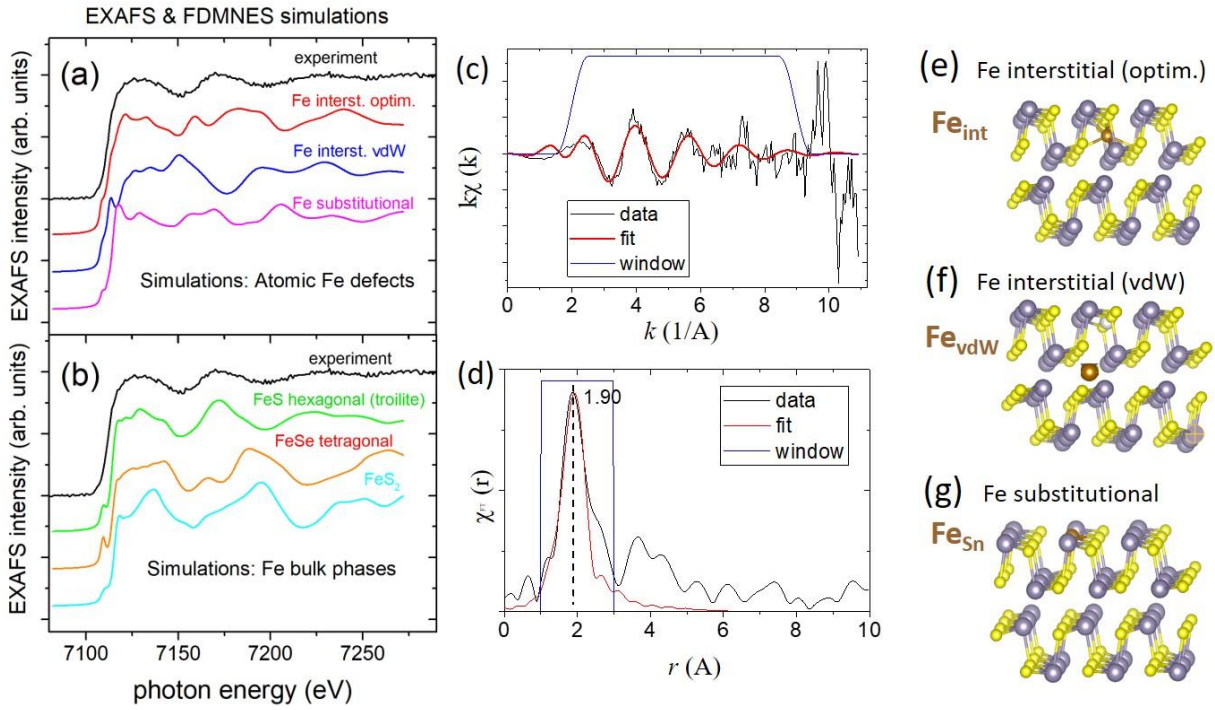

Figure 5: EXAFS experiment (a) and (b) along with simulations (FDMNES and FEFF codes) (c) and (d) for Fe at several positions within SnS structure (e) relaxed (energetically optimized) interstitial position Fe_i , (f) unrelaxed (structurally symmetric position) Fe_i and (g) substitutional defect, Fe_{Sn}.

In fact, the troilite phase of FeS was detected as segregated platelets by EBSD (see Fig. 4); however EDX analysis also indicated a significant amount of ~0.6% Fe atoms diluted in the SnS matrix. Thus, EXAFS suggests that diluted Fe preferentially forms a relaxed Fe_i in the vdW gap. However, we emphasize that other defects such as Fe_{Sn} or Fe_i complexes with V_S may be present in tin chalcogenide materials[25]. For example, an isolated Fe_{Sn} defect is surrounded by seven S-atoms with an atomic distance of less than 2.45 Å as detected by EXAFS. However, if one of the seven adjacent S atoms is missing (V_S), the Fe atom can strongly relax to a quasi-octahedral position surrounded by six NN S-atoms, leading to larger Fe-S distances.

Transport properties

Positive values of the Seebeck and the Hall coefficients indicate that the charge transport in the undoped SnS and $Sn_{0.99}Fe_{0.01}S$ SCs is dominated by holes (see Fig. 6). There is a general agreement that the dominant acceptors in p-type SnS are Sn vacancies - V_{Sn}^{-} [31]. According to published calculations[31,32] V_{Sn} has the lowest formation energy, suggesting that V_{Sn} is the dominant p-type defect under the S-rich SnS growth conditions. This defect was observed in STM experiments on FMC samples[25]. However, the number of electrically active vacancies $(V_{Sn}^{-} + h)$ may be reduced by the formation of di- or multivacancies $(V_{Sn}\text{-}V_{Sn}\text{-}\ldots)^{-\delta}$ owing to the dissolution of S_2 molecules in the SnS crystal[11]. These defects may correspond to the "mound-like" features in Ref. 25. Similar defects have also been recently reported in SnSe[33].

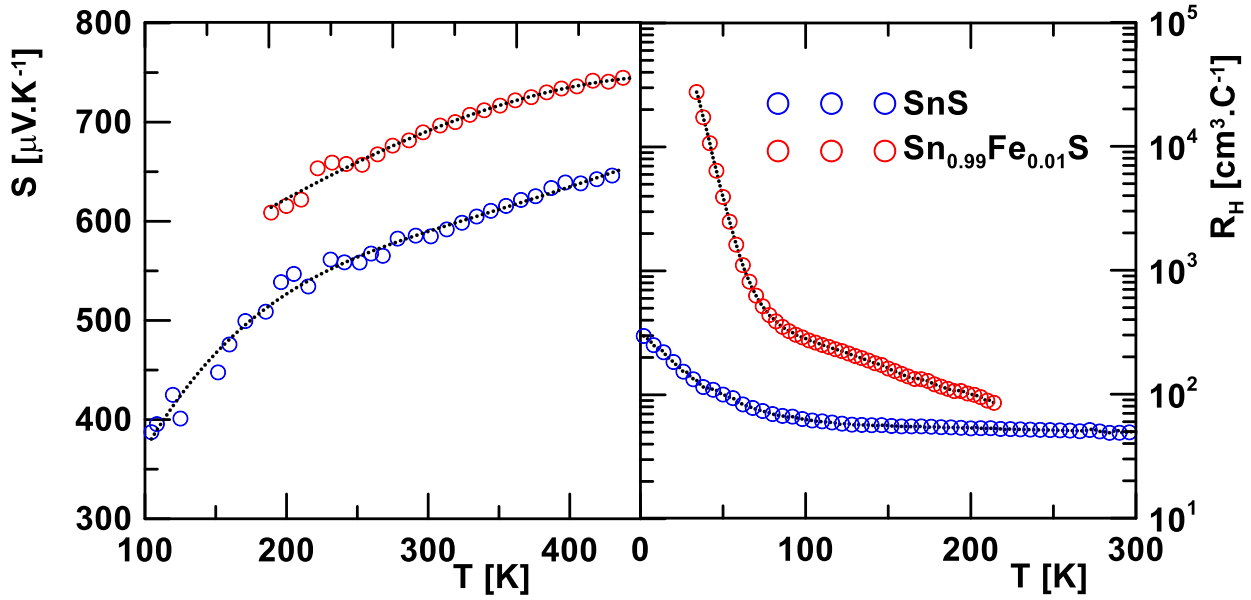

Fig 6: Seebeck coefficient and Hall coefficient of SnS and $Sn_{0.99}Fe_{0.01}S$ SCs as a function of temperature

The values of the defect activation energies can be derived from either the log ρ vs. 1000/T dependence - Arrhenius plot, $\rho = \rho_0 . \exp\left(\frac{E_a}{kT}\right)$ or from the dependence of the Hall concentration $1/(R_H.e)$ vs. 1000/T (Fig. 7b). However, a comparison of these two methods shows inconsistencies in terms of activation energies and the corresponding temperature regions (see Table 1). This discrepancy can be attributed to the fact that at least one type of electron and one type of hole are involved in charge transport.

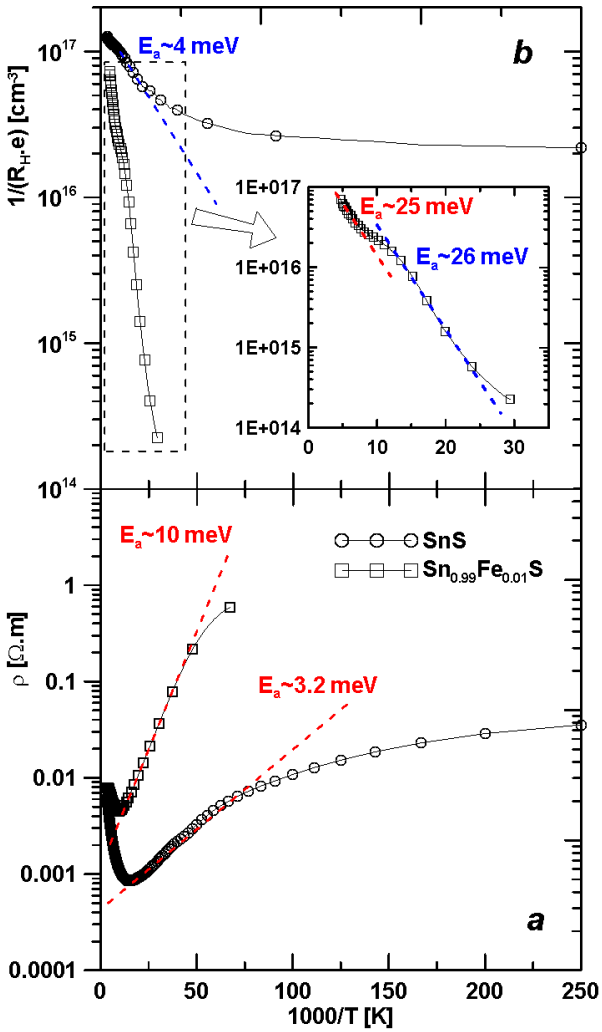

Fig.7: Dependences of the Hall concentration $1/(R_H.e)$ and the electrical resistivity ρ against the reciprocal temperature *1000/T* for the undoped SnS and $Sn_{0.99}Fe_{0.01}S$ sample.

Table 1: Table of activation energies obtained by fitting of r vs 1000/T and (1/R_He) vs 1000/T dependences using Arrhenius model with applied temperature range in parentheses.

Sample	Activation energy E_a [meV] (Temperature range [K])	
	ln ρ vs. 1/T	*ln (1/(R_H.e)) vs. 1/T*
SnS	3.2 (30-60 K)	4.0 (50-100 K)
$Sn_{0.99}Fe_{0.01}S$	10.0 (25-70 K)	26.0 (40 – 85 K)

Both electrons and holes were excited in overlapping temperature regions from/to shallow impurity energy levels below/above the CBM/VBM. As a result, the activation energies obtained represent a "mixture" of different contributions from different carrier types of specific concentrations and mobilities. In this case, the T-dependent $\rho(T)$ an $\frac{1}{R_H e}(T)$ can be expressed as follows:

$$\rho(T) = \frac{1}{\sigma(T)} = \frac{1}{e.[p(T).\mu_p(T)+n(T).\mu_n(T)]} \quad (1)$$

$$\frac{1}{R_H e}(T) = \frac{[p(T).\mu_p(T)+n(T).\mu_n(T)]^2}{p(T).\mu_p^2(T)-n(T).\mu_n^2(T)} = \frac{[p(T)+n(T).b(T)]^2}{p(T)-n(T).b^2(T)} \left(if\ b(T) = \frac{\mu_p(T)}{\mu_n(T)}\right), \quad (2)$$

where e is the charge of the electron, p and n are the hole and electron concentrations, respectively, and μ_p and μ_n are their mobilities. In addition, the situation seems to be further complicated by the possible involvement of variable-hopping mechanism (see SI Fig. S4) for at least one carrier type at low temperatures, similar to that of slightly doped SnSe[34].

In the literature on SnS crystals, sulfur vacancies V_S^+ [35,36] have also been reported in addition to vacancies V_{Sn}^-. The activation energies of these shallow defects lie close to VBM ($V_{Sn}^- - E_a \sim 21\ meV$) and CBM ($V_S^+ - E_a \sim 16\ meV$)[37]. However, other works[31,32,38] define the sulfur vacancy V_S as a deep-level defect, which rules out its donor activity in the low-temperature region. As far as donor activity is concerned, this leaves us with only the antisite defect Sn_S^+ which should have a very low formation energy under Sn-rich conditions[38]. We assume that small concentrations of SnS_2 and FeS foreign inclusions are insignificant in terms of charge transport properties.

Three different regions can be identified based on temperature-dependent resistivity. The low-temperature region; below *T*~30 K; is likely to be dominated by 3D Mott variable range hopping (VRH) (see SI Fig. S4). This is probably exclusively related to the existence of localized donor levels near the top of the valence band caused by the presence of V_{Sn} defects. In the middle region (30 - 60 K), a steep increase in the concentration (*1/(R_H.e)*) and resistivity ρ was observed. This reflects the thermal activation of the holes in the VB owing to the acceptor level. In addition to the acceptor level, the minor donor level can also be activated, which is probably related to the presence of Sn_S^+. In addition, it is possible that both mechanisms (VRH and activation) could be active simultaneously and form parallel conduction channels. Therefore, the activation energies obtained from either the dependence of lnρ *vs. 1000/T* or *1/(R_H.e) vs. 1000/T* represent the average values of the above excitations. Thus, it is difficult to discern the individual contributions of participating carrier types. The third region (above 60 K) indicates carrier saturation. It is

associated with a metallic behavior due to the electron–electron scattering within Fermi liquid theory, which occurs as shown by the ρ *vs.* T^2 dependence (see SI Fig. S5).

In contrast to the undoped sample, we observed a steep increase in the ρ- and R_H-values at low temperatures for the $Sn_{0.99}Fe_{0.01}S$ sample. The increase in the values is related to the substantial suppression of the total carrier concentration due to changes in the concentration of each type of point defect. In $Sn_{0.99}Fe_{0.01}S$, about half of the added Fe atoms were homogeneously distributed through the SC and interacted with native defects. STM observations showed that most of the Fe atoms enter interstitial positions Fe_i^+ and largely couple to acceptor-type V_{Sn}^- defects[25]. This leads to an almost one-order increase in the in-plane carrier mobility at low temperatures (~1000 $cm^2.V^{-1}.S^{-1}$ for SnS vs. ~8500 $cm^2.V^{-1}.S^{-1}$ for $Sn_{0.99}Fe_{0.01}S$ at 35 K).

One possible explanation is that the concentration of active acceptors – hole traps is significantly reduced due to doping. This would clearly increase the relaxation time and hole mobility. This, in turn, would indicate a rare situation – a kind of healing process due to doping. Such a healing process would correspond to a marked decrease of "mound-like" defects in[25], providing that these are active acceptors.

However, it cannot be ruled out that this increase in the hole mobility is only apparent. This may be related to the localization of minority electrons, which are presumably highly mobile, which would lead to the emptying of the conduction band. The localization of electrons is related to the change in the structure of the defects due to doping - e.g., the disappearance of Sn_S^+ or the formation of complex defects $(Fe_i^+ V_{Sn}^-)$. However, the most significant culprit is sulfur vacancies, V_S, which are present in the Fe-doped sample but not in the undoped sample[25]. Specifically, V_S is a deep donor capable of electrons capture[17]. Thus, a smaller number of electrons would be involved in the transport, leading to a virtual increase in the Hall coefficient, and hence, the Hall mobility, according to Eq. 2. Thus, Fe doping would, in fact, only reveal the true magnitude of hole mobility in SnS. Therefore, we argue that the mobility may have a similar magnitude in undoped SnS, but the measured value may not be realistic because of the mixed transport of electrons and holes (Equations 1 and 2). This conclusion is also supported by the fact that both the doped and undoped samples show a similar concentration of point defects in STM experiments[25].

In addition, the carrier mobility in the doped sample may be reduced owing to the increased mosaicity compared with the undoped sample (Fig. 2). This implies that the actual hole mobility may be even higher in the undoped sample with negligible mosaicity. These findings are consistent with the formation of SnS_2 in Fe-doped SC. Specifically, the formation of SnS_2 is logically related to

S-rich conditions, which is in turn associated with an increase in the formation energy and a decrease in the concentration of Sn_S^+. This probably excludes the minority carriers (electrons) from charge transport and shifts the activation energies towards more realistic values that correspond to the activation of holes (see Fig. 7); cf. e.g., the activation energy of tin vacancies - V_{Sn}^-, E_a=21 meV in [37].

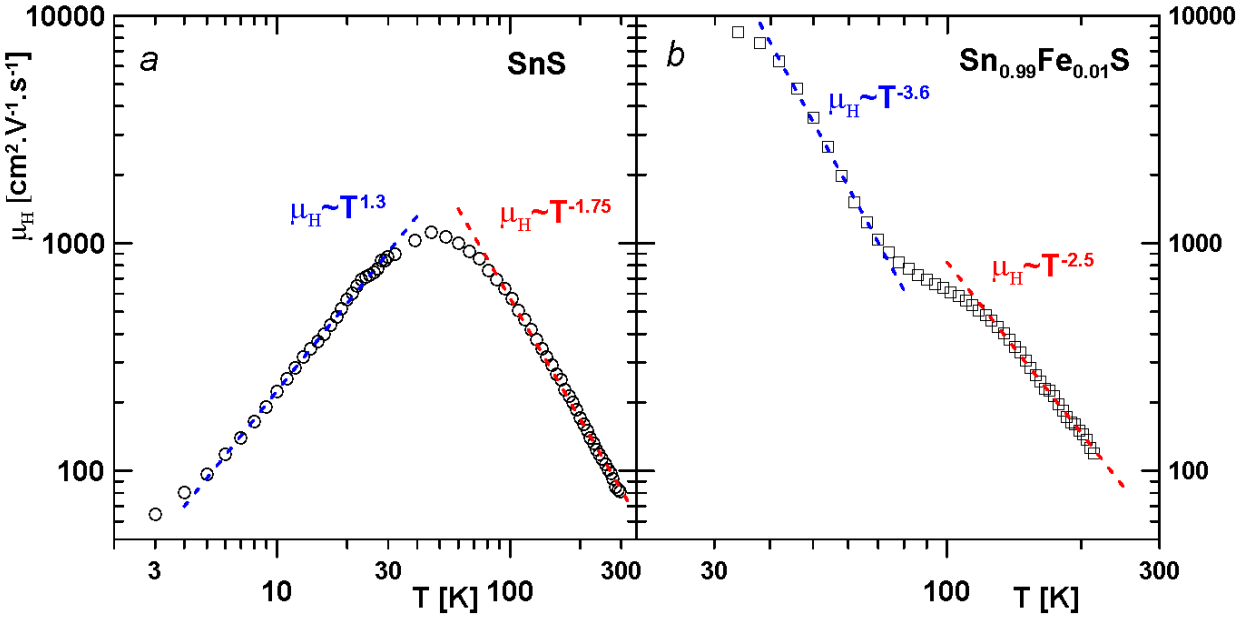

Fig. 8: Dependences of the Hall mobility R_H/ρ and the electrical resistivity ρ on the inverse of temperature 1000/T for undoped SnS (a) and $Sn_{0.99}Fe_{0.01}S$ (b) sample.

The difference between the activation energies derived from the resistivity (E_a~26 meV) and Hall (E_a~10 meV) measurements results from the combination of the VRH and band conduction in the overlapping temperature regions.

The slope of the mobility dependence on temperature - $\mu_H \sim T^n$ (Fig. 8 a,b) was used to reveal the mechanism of charge carrier scattering within the exponent n. In the low-temperature region (T<30 K), scattering is dominated by ionized impurities $(n \approx 1.5)$ for the undoped SnS SC. Unfortunately, we could not obtain this information for the $Sn_{0.99}Fe_{0.01}S$ SC because of the very high resistivity of the sample. At higher temperatures (above 30 K), dominant scattering occurs on homopolar optical phonons $(-n > 1)$ which is intrinsic to layered materials[39,40]. Thus, we consider scattering on homopolar optical phonon to be the main scattering process controlling the in-plane transport of charge carriers at these temperatures, which is consistent with conclusions made for SnSe[41].

Conclusions

A broad characterization of Fe-doped SnS single crystals showed that the properties of this type of material strongly depend on the particular defect structure of the crystal. Even very small amounts of dopants fundamentally changed the charge-transport properties. This is related to the interaction of doping impurities with native defects, for example, the formation of complex defects ($Fe_i + V_{Sn}$). Specifically, this interaction leads to electron localization, which in the case of Fe doping, empties the conduction band. This, in turn, allows in some cases the investigation of pure hole transport. Importantly, this study suggests that hole mobility in SnS may be relatively insensitive to certain types of doping. Such defect insensitive mobility is important for all potential applications. Interestingly, the Hall mobility remains high despite the significant mosaicity of the doped sample and despite the fact that Fe incorporation is quite heterogeneous with foreign phases forming in addition to point defects for all doping concentrations. This observation is made possible by the fact that at higher temperatures the dominant scattering is on the homopolar optical modes of the phonon spectrum.

Acknowledgments

This work was supported by the Czech Science Foundation Grant No. 19-13659S. We acknowledge CzechNanoLab and MGML Research Infrastructures (LM2023051 and LM2023065, respectively) and project SOLID21 (CZ.02.1.01/0.0/0.0/16_019/0000760), all supported by MEYS CR. The assistance of Juraj Krempaský (SLS, PSI, Switzerland) with X-ray absorption measurement is greatly acknowledged.

Data availability

Data will be made available on request.

References

[1] Z. Li, Y. Guo, F. Zhao, C. Nie, H. Li, J. Shi, X. Liu, J. Jiang, S. Zuo, Effect of film thickness and evaporation rate on co-evaporated SnSe thin films for photovoltaic applications, RSC Adv. 10 (2020) 16749–16755. https://doi.org/10.1039/d0ra01749c.

[2] F. Kawamura, Y. Song, H. Murata, H. Tampo, T. Nagai, T. Koida, M. Imura, N. Yamada, Tunability of the bandgap of SnS by variation of the cell volume by alloying with A.E. elements, Sci. Rep. 12 (2022) 7434 (1–9). https://doi.org/10.1038/s41598-022-11074-2.

[3] S.F. Wang, W. Wang, W.K. Fong, Y. Yu, C. Surya, Tin Compensation for the SnS Based Optoelectronic Devices, Sci. Rep. 7 (2017) 39704 (1–10). https://doi.org/10.1038/srep39704.

[4] M. Kumar, S. Rani, P. Vashishtha, G. Gupta, X. Wang, V.N. Singh, Exploring the optoelectronic properties of SnSe: a new insight, J. Mater. Chem. C. (2022) 16714–16722. https://doi.org/10.1039/d2tc03799h.

[5] S. Harish, P.U. Sathyakam, A review of tin selenide-based electrodes for rechargeable batteries and supercapacitors, J. Energy Storage. 52 (2022) 104966. https://doi.org/10.1016/j.est.2022.104966.

[6] M.A. Dar, D. Govindarajan, G.N. Dar, Facile synthesis of SnS nanostructures with different morphologies for supercapacitor and dye-sensitized solar cell applications, J. Mater. Sci. Mater. Electron. 32 (2021) 20394–20409. https://doi.org/10.1007/s10854-021-06550-w.

[7] W. He, D. Wang, J.F. Dong, Y. Qiu, L. Fu, Y. Feng, Y. Hao, G. Wang, J. Wang, C. Liu, J.F. Li, J. He, L.D. Zhao, Remarkable electron and phonon band structures lead to a high thermoelectric performance: ZT > 1 in earth-abundant and eco-friendly SnS crystals, J. Mater. Chem. A. 6 (2018) 10048–10056. https://doi.org/10.1039/c8ta03150a.

[8] C. Zhou, Y.K. Lee, Y. Yu, S. Byun, Z.Z. Luo, H. Lee, B. Ge, Y.L. Lee, X. Chen, J.Y. Lee, O. Cojocaru-Mirédin, H. Chang, J. Im, S.P. Cho, M. Wuttig, V.P. Dravid, M.G. Kanatzidis, I. Chung, Polycrystalline SnSe with a thermoelectric figure of merit greater than the single crystal, Nat. Mater. 20 (2021) 1378–1384. https://doi.org/10.1038/s41563-021-01064-6.

[9] F. Li, H. Wang, R. Huang, W. Chen, H. Zhang, Recent Advances in SnSe Nanostructures beyond Thermoelectricity, Adv. Funct. Mater. 32 (2022) 1–63. https://doi.org/10.1002/adfm.202200516.

[10] L.D. Zhao, S.H. Lo, Y. Zhang, H. Sun, G. Tan, C. Uher, C. Wolverton, V.P. Dravid, M.G. Kanatzidis, Ultralow thermal conductivity and high thermoelectric figure of merit in SnSe crystals, Nature. 508 (2014) 373–377. https://doi.org/10.1038/nature13184.

[11] W. Albers, C. Haas, H.J. Vink, J.D. Wasscher, Investigations on SnS, J. Appl. Phys. 32 (1961) 2220–2225. https://doi.org/10.1063/1.1777047.

[12] W. Albers, C. Haas, F. van der Maesen, The preparation and the electrical and optical properties of SnS crystals, J. Phys. Chem. Solids. 15 (1960) 306–310. https://doi.org/10.1016/0022-3697(60)90253-5.

[13] A. Jannat, F. Haque, K. Xu, C. Zhou, B.Y. Zhang, N. Syed, M. Mohiuddin, K.A. Messalea, X. Li, S.L. Gras, X. Wen, Z. Fei, E. Haque, S. Walia, T. Daeneke, A. Zavabeti, J.Z. Ou, Exciton-Driven Chemical Sensors Based on Excitation-Dependent Photoluminescent Two-Dimensional SnS, ACS Appl. Mater. Interfaces. 11 (2019) 42462–42468. https://doi.org/10.1021/acsami.9b12843.

[14] J.N. Olding, A. Henning, J.T. Dong, Q. Zhou, M.J. Moody, P.J.M. Smeets, P. Darancet, E.A. Weiss, L.J. Lauhon, Charge Separation in Epitaxial SnS/MoS_2 Vertical Heterojunctions Grown by Lowerature Pulsed MOCVD, ACS Appl. Mater. Interfaces. 11 (2019) 40543–40550. https://doi.org/10.1021/acsami.9b14412.

[15] S. Li, Y. Wang, P. Cheng, B. Feng, L. Chen, K. Wu, Realization of Large Scale, 2D van der Waals Heterojunction of SnS_2/SnS by Reversible Sulfurization, Small. 17 (2021) 1–8. https://doi.org/10.1002/smll.202101154.

[16] I. Suzuki, S. Kawanishi, T. Omata, H. Yanagi, Current status of n-type SnS: Paving the way for SnS homojunction solar cells, JPhys Energy. 4 (2022). https://doi.org/10.1088/2515-7655/ac86a1.

[17] F.Y. Ran, Z. Xiao, Y. Toda, H. Hiramatsu, H. Hosono, T. Kamiya, N-type conversion of SnS by isovalent ion substitution: Geometrical doping as a new doping route, Sci. Rep. 5 (2015) 1–8. https://doi.org/10.1038/srep10428.

[18] F. Wang, L. Zhou, Z. Ma, M. He, F. Wu, Y. Liu, First-principles investigations of magnetic semiconductors: An example of transition metal decorated two-dimensional SnS monolayer, Nanomaterials. 8 (2018). https://doi.org/10.3390/nano8100789.

[19] C. Tang, Q. Li, C. Zhang, C. He, J. Li, T. Ouyang, H. Li, J. Zhong, Stability and magnetic properties of SnSe monolayer doped by transition metal atom (Mn, Fe, and Co): A first-principles study, J. Phys. D. Appl. Phys. 51 (2018). https://doi.org/10.1088/1361-6463/aac3eb.

[20] A.A. Tedstone, D.J. Lewis, P. O'Brien, Synthesis, Properties, and Applications of Transition Metal-Doped Layered Transition Metal Dichalcogenides, Chem. Mater. 28 (2016) 1965–1974. https://doi.org/10.1021/acs.chemmater.6b00430.

[21] H. Yang, L.G. Liu, M. Zhang, X.S. Yang, Growth and magnetic properties of Ni-doped Bi_2Se_3 topological insulator crystals, Solid State Commun. 241 (2016) 26–31. https://doi.org/10.1016/j.ssc.2016.05.008.

[22] M. Zhang, L. Liu, H. Yang, Anomalous second ferromagnetic phase transition in $Co_{0.08}Bi_{1.92}Se_3$ topological insulator, J. Alloys Compd. 678 (2016) 463–467. https://doi.org/10.1016/j.jallcom.2016.04.023.

[23] J.B. Vaney, S. Aminorroaya Yamini, H. Takaki, K. Kobayashi, N. Kobayashi, T. Mori, Magnetism-mediated thermoelectric performance of the Cr-doped bismuth telluride tetradymite, Mater. Today Phys. 9 (2019) 100090. https://doi.org/10.1016/j.mtphys.2019.03.004.

[24] R. Vasudevan, L. Zhang, Q. Ren, J. Wu, Z. Cheng, J. Wang, S. Lin, F. Zhu, Y. Zhang, M. Hölzel, Y. Pei, X. Tong, J. Ma, Secondary phase effect on the thermoelectricity by doping Ag in SnSe, J. Alloys Compd. 923 (2022). https://doi.org/10.1016/j.jallcom.2022.166251.

[25] D. Yesilpinar, M. Vondráček, P. Čermák, H. Mönig, J. Kopeček, O. Caha, K. Carva, Č. Drašar, J. Honolka, Defect pairing in Fe-doped SnS van der Waals crystals: a photoemission and scanning tunneling microscopy study, Nanoscale. 15 (2023) 13110–13119. https://doi.org/10.1039/d3nr01905e.

[26] E. Sutter, J. Wang, P. Sutter, Surface Passivation by Excess Sulfur for Controlled Synthesis of Large, Thin SnS Flakes, Chem. Mater. 32 (2020) 8034–8042. https://doi.org/10.1021/acs.chemmater.0c03297.

[27] M. Ristov, I. Sinadinovski, I. Grozdanov, M. Mitreski, Chemical Deposition of Tin (II) Sulphide Thin Films, Thin Solid Films. 173 (1989) 53–58.

[28] B. Parveen, M. Hassan, S. Riaz, S. Atiq, S. Naseem, M. Irfan, M.F. Iqbal, Investigation of physical properties of SnS:Fe diluted magnetic semiconductor nanoparticles for spintronic applications, J. Magn. Magn. Mater. 460 (2018) 111–119. https://doi.org/10.1016/j.jmmm.2018.03.022.

[29] J. Cuda, T. Kohout, J. Tucek, J. Haloda, J. Filip, R. Prucek, R. Zboril, Low-temperature magnetic transition in troilite: A simple marker for highly stoichiometric FeS systems, J. Geophys. Res. Solid Earth. 116 (2011) 1–9. https://doi.org/10.1029/2011JB008232.

[30] T. Kohout, A. Kosterov, M. Jackson, L.J. Pesonen, G. Kletetschka, M. Lehtinen, Low-temperature magnetic properties of the Neuschwanstein EL6 meteorite, Earth Planet. Sci. Lett. 261 (2007) 143–151. https://doi.org/10.1016/j.epsl.2007.06.022.

[31] J. Vidal, S. Lany, M. D'Avezac, A. Zunger, A. Zakutayev, J. Francis, J. Tate, Band-structure, optical properties, and defect physics of the photovoltaic semiconductor SnS, Appl. Phys. Lett. 100 (2012). https://doi.org/10.1063/1.3675880.

[32] L.A. Burton, D. Colombara, R.D. Abellon, F.C. Grozema, L.M. Peter, T.J. Savenije, G. Dennler, A. Walsh, Synthesis, Characterization, and Electronic Structure of Single- Crystal SnS, Sn_2S_3, and SnS_2, Chem. Mater. 25 (2013) 4908–4916. https://doi.org/10.1021/cm403046m.

[33] V.Q. Nguyen, T.L. Trinh, C. Chang, L.D. Zhao, T.H. Nguyen, V.T. Duong, A.T. Duong, J.H. Park, S. Park, J. Kim, S. Cho, Unidentified major p-type source in SnSe: Multivacancies, NPG Asia Mater. 14 (2022). https://doi.org/10.1038/s41427-022-00393-5.

[34] M. Zorić, N.S. Dhami, K. Bader, P. Gille, A. Smontara, P. Popčević, Negative Magnetoresistance in Hopping Regime of Lightly Doped Thermoelectric SnSe, Materials (Basel). 16 (2023). https://doi.org/10.3390/ma16072863.

[35] Y. Yin, J. Cai, H. Wang, Y. Xiao, H. Hu, X. Tan, G.Q. Liu, J. Jiang, Single-crystal growth of n-type $SnS_{0.95}$ by the temperature-gradient technique, Vacuum. 182 (2020) 109789. https://doi.org/10.1016/j.vacuum.2020.109789.

[36] Z. Xiao, F.Y. Ran, H. Hosono, T. Kamiya, Route to n -type doping in SnS, Appl. Phys. Lett. 106 (2015) 1–5. https://doi.org/10.1063/1.4918294.

[37] N. Spalatu, J. Hiie, R. Kaupmees, O. Volobujeva, J. Krustok, I.O. Acik, M. Krunks, Postdeposition Processing of SnS Thin Films and Solar Cells: Prospective Strategy to Obtain Large, Sintered, and Doped SnS Grains by Recrystallization in the Presence of a Metal Halide Flux, ACS Appl. Mater. Interfaces. 11 (2019) 17539–17554. https://doi.org/10.1021/acsami.9b03213.

[38] Y. Kumagai, L.A. Burton, A. Walsh, F. Oba, Electronic Structure and Defect Physics of Tin Sulfides: SnS, Sn_2S_3, and SnS_2, Phys. Rev. Appl. 6 (2016) 1–14. https://doi.org/10.1103/PhysRevApplied.6.014009.

[39] L. Tichý, J. Horák, Nonparabolicity of the conduction band and anisotropy of the electron effective mass in n-Bi_2Se_3 single crystals, Phys. Rev. B. 19 (1979) 1126–1131. https://doi.org/10.1103/PhysRevB.19.1126.

[40] R. Fivaz, E. Mooser, Mobility of charge carriers in semiconducting layer structures, Phys. Rev. 163 (1967) 743–755. https://doi.org/10.1103/PhysRev.163.743.

[41] C.K. Sumesh, M. Patel, K.D. Patel, G.K. Solanki, V.M. Pathak, R. Srivastav, Low temperature electrical transport properties in p-SnSe single crystals, EPJ Appl. Phys. 53 (2011) 3–7. https://doi.org/10.1051/epjap/2010100383.